Fusion Pore Dynamics and Insulin Granule Exocytosis in the Pancreatic Islet

Noriko Takahashi,[1] Takuya Kishimoto,[1] Tomomi Nemoto,[1] Takashi Kadowaki,[2] Haruo Kasai[1]*

Insulin secretion from intact mouse pancreatic islets was investigated with two-photon excitation imaging. Insulin granule exocytosis occurred mainly toward the interstitial space, away from blood vessels. The fusion pore was unusually stable with a lifetime of 1.8 seconds. Opening of the 1.4-nanometer-diameter pore was preceded by unrestricted lateral diffusion of lipids along the inner wall of the pore, supporting the idea that this structure is composed of membrane lipids. When the pore dilated to 12 nanometers, the granules rapidly flattened and discharged their contents. Thus, our methodology reveals fusion pore dynamics in intact tissues at nanometer resolution.

The secretion of hormones and neurotransmitters has been studied intensively by measurement of membrane capacitance and amperometry (*1*). Secretion occurs by exocytosis, in which the secretory vesicle and plasma membranes merge, causing release of the vesicular contents (*1*). Exocytosis begins with the formation of a semistable fusion pore with a diameter of ~1.5 nm that connects secretory granules and the extracellular space (*2*–*5*). These electrophysiological approaches, however, are applicable only to specific preparations, consisting mostly of isolated cells, that fulfill their stringent requirements (*2*–*5*). It is also impossible with these techniques to trace the vesicles after expansion of the pore. Although, in principle, exocytosis is amenable to study by electron microscopy, exocytotic events are detected infrequently and with poor time resolution with this approach (*6*, *7*). Moreover, it is not possible to examine fusion pores with diameters of <4 nm even by freeze fracture (*8*, *9*). Such technical difficulties have prevented characterization of the properties of fusion pores, and their molecular composition remains unclear (*10*).

We have visualized intercellular spaces inside living pancreatic islets with a solution containing a fluid-phase tracer, sulforhodamine B (SRB, 0.7 mM), using two-photon excitation imaging (*11*, *12*), which can effectively avoid the inner filter effect of the bright fluorescent tracer (*13*). Three-dimensional (3D) reconstruction of the images revealed a few major vessels and numerous tubular capillaries surrounding the endocrine cells (movie S1). In the 2D images, major vessels appeared as bright regions and capillaries as small bright spots around a cell (Fig. 1A). Stimulation of islets with a high concentration (20 mM) of glucose in the continuous presence of SRB resulted in the abrupt appearance and gradual waning of discrete fluorescent spots adjacent to the plasma membrane of cells (Fig. 1, B to D) (movie S2).

Several observations indicate that the transient fluorescent spots represented the fusion of individual insulin granules with the plasma membrane of β cells and the subsequent flattening of the granules: (i) The diameter of the spots ranged between 0.28 and 0.7 μm, with a mean value of 0.47 μm (n = 167), which is consistent with the mean diameter (0.45 μm, n = 47) of individual insulin granules stained with antibodies to insulin. Moreover, the spots stained with a fixable fluid-phase tracer, either Lucifer yellow or 3-kD fluorescein-dextran, proved to be insulin positive (Lucifer yellow, 28/38 spots; fluorescein-dextran, 12/40 spots) (Fig. 1E). (ii) Most cells in the second to fourth layers of islets were responsive to glucose (Fig. 2A), consistent with the abundance of β cells within islets. (iii) The time of appearance of the spots was precisely correlated with the glucose-induced increase in the cytosolic concentration of Ca^{2+} (Fig. 2B) (*14*). (iv) Forskolin, which induces the cytosolic accumulation of adenosine 3′,5′-monophosphate (cAMP), markedly increased the number of events without substantially affecting the increase in the cytosolic Ca^{2+} concentration (Fig. 2C) (*14*, *15*). (v) The number of events during the first phase of glucose-induced insulin secretion was estimated to be 13 per cell per minute (*12*), consistent with radioimmunoassay (*12*). Thus, our imaging strategy allows visualization of most insulin exocytotic events in the plane of focus.

Insulin secretion has been thought to occur in the "advascular" compartment (that facing

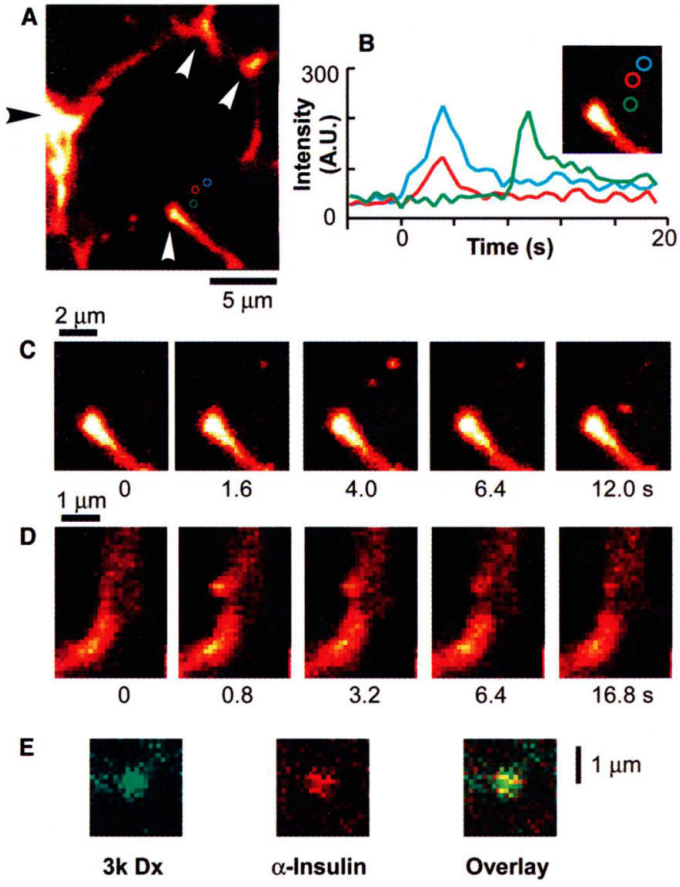

Fig. 1. Two-photon excitation imaging of exocytotic events in β cells within mouse pancreatic islets. (**A**) Single β cell in which SRB fluorescent spots appeared during high-glucose stimulation (Movie S2). Black arrowhead indicates a major vessel, and white arrowheads indicate microvessels. The image is the first frame of movie S2. (**B**) Time courses of SRB fluorescence (A.U., arbitrary units) measured at the three regions indicated by circles in the inset and in (A). (**C** and **D**) Successive images of the glucose-induced abrupt appearance of SRB fluorescent spots. The images in (C) were obtained from the region adjacent to the interstitial space shown in (B); those in (D) show the secretory granule coalescing with the plasma membrane. (**E**) Example of a fused granule that was labeled with 3-kD fluorescein-dextran (3k Dx), fixed, and stained with antibodies to insulin (α-Insulin).

[1]Department of Cell Physiology, National Institute for Physiological Sciences, and the Graduate University of Advanced Studies, Myodaiji, Okazaki 444-8585, Japan. [2]Department of Metabolic Diseases, Graduate School of Medicine, University of Tokyo, 7-3-1 Hongo, Bunkyo-ku, Tokyo 113-8655, Japan.

*To whom correspondence should be addressed. E-mail: hkasai@nips.ac.jp

blood vessels) of β cells (*16*). However, our imaging data revealed that most exocytotic events (mean ± SD, 71 ± 7%; $n = 8$) occurred in the "abvascular" compartment (Fig. 2, A and D): Overall, ~60% of the β-cell surface participated in exocytosis, as in single cells (*17*). We still detected a polarity of β cells (Fig. 2A): Exocytosis occurred preferentially in the vicinity of certain vessels, possibly veins, around which β cells appear to form rosettes (*18*). Some cells exhibited exocytotic events only during the first or the second phase of secretion (Fig. 2, A and E), indicating intra-islet heterogeneity (*19*, *20*).

We next assessed fusion pore dynamics simultaneously using the fluid-phase tracer SRB and a membrane tracer, FM1-43 (20 μM) (*21*). FM1-43 is an amphiphilic dye that fluoresces only when it is inserted into a membrane, but it does not cross a membrane bilayer. Consequently, it can readily stain the plasma membranes deep in the islets (*22*). The FM1-43 signal at the site of SRB events (Fig. 3A) was consistent with the selective staining of the granule membrane but not the granule matrix in mouse β cells (*12*). Unexpectedly, the FM 1-43 signal appeared simultaneously with or slightly preceded the SRB signal (Fig. 3, A and B), with a latency of the latter being 0 to 2 s (mean ± SD, 0.31 ± 0.60 s; $n = 65$). The large flux of FM1-43 thus occurred already at the onset of staining with SRB (Fig. 3C). Moreover, FM1-43 stained granules more rapidly, with a time constant of 0.4 s (Fig. 3C), than did SRB, for which staining did not reach a plateau within the few seconds before it started to decay (Fig. 3, A and C).

The staining of granule membrane with FM1-43 might result either from aqueous permeation of FM1-43 through the fusion pore and its subsequent insertion into the granule membrane, or from lateral diffusion of FM1-43 from already stained membrane through the inner wall of the fusion pore (fig. S1, A and B). Three observations support the latter scenario: (i) Because the molecular size of FM1-43 is similar to that of SRB, the earlier onset of the FM1-43 signal relative to the SRB signal (Figs. 3B and 4, A and B; see supporting online material) is inconsistent with permeation of both molecules through the same aqueous pore (fig. S1A). (ii) If aqueous permeation is the predominant mechanism of such staining, the time constant of granule staining should depend on the concentration of FM1-43 (Fig. 3D, dashed line), given that aqueous inflow is proportional to dye concentration (fig. S1B) and that FM1-43 staining of the membrane was saturable with a dissociation constant of 7 μM (*12*). However, the time constant was independent of the concentration of FM1-43 between 5 and 50 μM (Fig. 3, C and D) (*12*). (iii) The aqueous permeation mechanism predicts that FM1-43 staining should be slower than SRB staining, given that the granule membrane accumulates 16 times the number of molecules present in the aqueous phase of a granule (*12*). We obtained the opposite result (Fig. 3, C and D). Thus, the time constant of staining can be approximated by $4\pi R^2/(2\pi r D_m/L)$, the granule membrane area divided by the influx of FM1-43 along the inner wall of the pore (fig. S1, A and B), where R is the granule radius; r and l are the radius and length of the fusion pore, respectively; and D_m is the lateral diffusion constant of FM1-43. This approximation is valid because the pore was stable, as described below. The observed time constant of 0.4 s yields an estimate of the lateral diffusion constant (D_m) for FM1-43 of 3.3 μm^2 s^{-1} (at $2R = 0.43$ μm, $2r = 1.4$ nm, and $L = 10$ nm), which is larger than that for lipids in the plasma membrane (<1 μm^2 s^{-1}) and similar to that of pure lipid bilayers (1 to 10 μm^2 s^{-1}) (*23*).

We next probed expansion of the fusion pore with tracers of various molecular sizes (*12*). The smaller molecules, SRB (~1.4 nm) and 3-kD dextran (~4 nm), permeated earlier than did 10-kD dextran (~6 nm), whereas 70-kD dextran (~12 nm) permeated later (Fig. 4B, C, and E). As expected, two 10-kD dextran tracers permeated simultaneously (Fig. 4D). The observation that the larger tracers began to permeate abrupt-

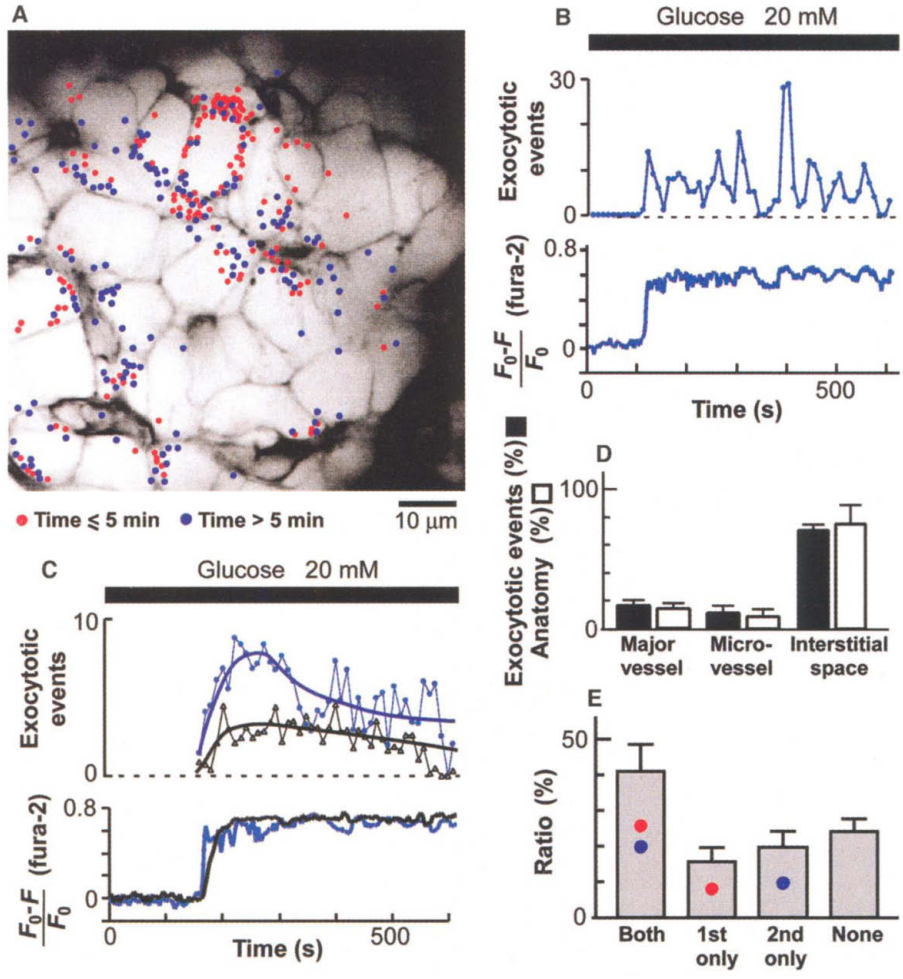

Fig. 2. Spatiotemporal distribution of exocytotic events in pancreatic islets. (**A**) Distribution of exocytotic events in an islet stimulated with 20 mM glucose. Red and blue dots represent sites at which exocytotic events were observed in the first and second phases of glucose-induced insulin secretion, respectively. The underlying gray image is the inverse image of SRB fluorescence. (**B** and **C**) Glucose-induced exocytosis in a single islet (B) or averaged for several islets (C). Data in (C) were acquired from islets treated in the absence (black, $n = 5$) or presence (blue, $n = 3$) of forskolin. Exocytotic events were measured within an arbitrary area (2000 μm^2) of islets. The bottom traces show the increase in the cytosolic Ca^{2+} concentration recorded from a single islet. The cytosolic Ca^{2+} concentration is represented by $(F_0 - F)/F_0$, where F_0 and F stand for resting and poststimulation fluorescence, respectively. (**D**) Distribution of exocytotic events (filled bars) in the regions of cells that face major vessels, microvessels, or the interstitial space and the proportional areas of these three distinct regions (open bars). The histogram was constructed from 1231 events in 174 cells of eight islets. (**E**) Proportion of cells (216 cells in 9 islets) that exhibited exocytosis in both phases (red and blue dots), only in the first phase (red dot), or only in the second phase (blue dot) of glucose-induced insulin secretion. Errors bars in (D) and (E) represent the SEM among islets. Data obtained with preparations incubated in the absence of forskolin did not differ significantly from those obtained with islets exposed to this drug and were therefore included in (D) and (E).

ly after the smaller tracers suggests that the expanding pore has a well-defined geometry. Moreover, closure of the SRB-permeable pore was detected without opening of the 10-kD dextran-permeable pore in 7% (11/164) of SRB events, which were characterized by smaller increases in SRB fluorescence (*12*) that ceased shortly after pore opening (Fig. 4F). Such closure was also detected in 2% (2/84) of 3-kD dextran events before 10-kD dextran events, but not in 10-kD dextran events before 70-kD dextran events (n = 62). Thus, the fusion pore was semistable when the pore diameter was between 1.4 and 4 nm, corresponding to a conductance of 140 pS to 0.97 nS (*12*) and consistent with capacitance measurements (*2–4*).

The lifetime of the fusion pore quantified with SRB and 10-kD dextran varied between 0 and 4 s, with a mean ± SD of 1.8 ± 0.8 s (n = 65) (Fig. 4B). This lifetime is longer than those estimated for adrenal chromaffin cells (0.052 s) (*5*), mast cells (0.058 s), and beige mast cells (0.36 s) (*4*) from capacitance measurements. We confirmed that our imaging technique yielded a short lifetime in chromaffin cell clusters (0.041 s, n = 52) (Fig. 4B, hatched bar). We hypothesized that the unusually long lifetime of the fusion pore of insulin granules might be due to the crystalline nature of the packaged insulin, which may retard granule swelling and expansion of the fusion pore (*24*). To test this notion, we examined β cells of the guinea pig, in which insulin is crystallized to a reduced extent as a result of a mutation in the amino acid sequence (*25*). We found that 50% of the insulin granules exhibited short lifetimes that were rarely seen in mice (Fig. 4B, gray bars), with the mean (± SD) lifetime of the pore being only 0.58 ± 0.65 s (n = 57). In contrast, when we added Zn (2 mM) to extracellular solution to prevent the dissolution of insulin crystal in mice islets, the lifetime was prolonged to 3.5 ± 1.2 s (n = 28).

The decay in SRB fluorescence (Figs. 1B and 3A) represented the full collapse of granules into the plasma membrane and resulting discharge of the granular contents (Fig. 1D; fig. S2 and supporting online text). The reduction in SRB fluorescence always began soon (0.2 ± 0.4 s, n = 131) after the opening of the large pore (~12 nm) that allowed the permeation of 70-kD dextran (Fig. 4, G and H), suggesting that granule flattening occurs when the fusion pore begins to allow the passage of large-size granule contents, such as insulin hexamers (36 kD) (*26*).

Thus, most insulin secretion is abvascular and associated with granule flattening in β cells in the islet. The rare ultrastructural observation of exocytosis (*6*) can now be explained by the short lifetime (2 to 3 s) of fused granules with a large pore diameter (>4 nm). The lack of tight junctions between cells in islets (*27*) may enhance the

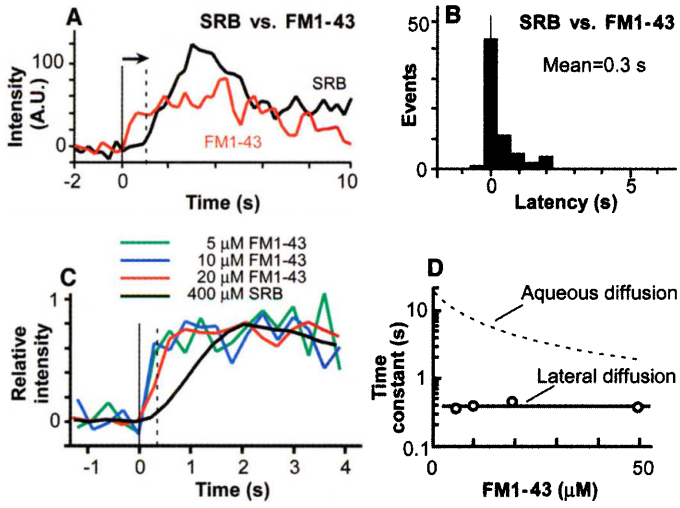

Fig. 3. Simultaneous imaging of exocytosis with the aqueous tracer SRB and the lipid tracer FM1-43. (**A**) Example of the time courses of FM1-43 (red) and SRB (black) staining of an insulin granule within a β cell of a mouse pancreatic islet. (**B**) Latency distribution for the onset of SRB staining relative to that of FM1-43 staining. (**C**) Averaged time courses of FM1-43 (color) and SRB (black) fluorescence acquired from the same granules. The traces are aligned at the onset of the FM1-43 signal. The red, blue, and green lines represent the fluorescence of FM1-43 at 20 μM (n = 11), 10 μM (n = 7), and 5 μM (n = 7), respectively. Solid and dashed vertical lines indicate the onsets of FM1-43 and SRB staining, respectively, in (A) and (C). (**D**) Concentration dependence of the time constant (circles) of granule staining with FM1-43. The solid line represents theoretical estimates with a lateral diffusion constant (D_m) of 3.3 μm^2 s^{-1}. The dashed line is predicted from the aqueous diffusion of FM1-43 through the fusion pore with an aqueous diffusion constant (D_{aq}) of 500 μm^2 s^{-1} (*12*).

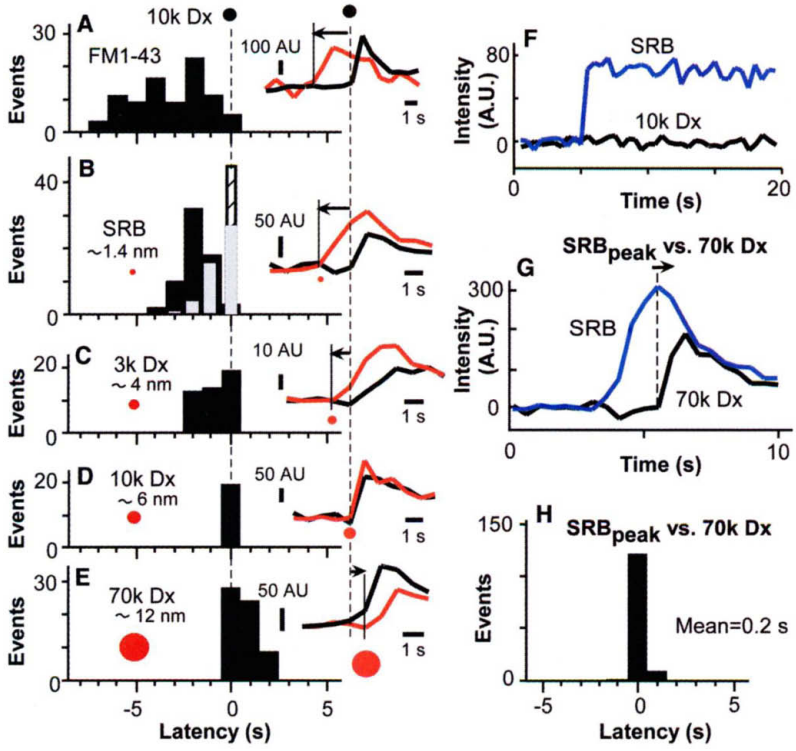

Fig. 4. Dynamics of fusion pore opening. (**A** to **E**) Latency histograms for the onset of staining with various dyes relative to that of staining with 10-kD dextran (10k Dx) dyes: FM1-43 versus 10-kD Texas red–dextran (A), SRB versus 10-kD fluorescein-dextran (B), 3-kD Texas red–dextran versus 10-kD Alexa Fluor 488–dextran (C), 10-kD Texas red–dextran versus 10-kD Alexa Fluor 488–dextran (D), and 70-kD Texas red–dextran versus 10-kD Alexa Fluor 488–dextran (E). Insets show examples of simultaneously measured fluorescence of the two tracers; each pair of traces was obtained from a single insulin granule within a β cell of a mouse pancreatic islet. Solid and dashed vertical lines indicate the onsets of staining with the two tracers as indicated. Gray bars in (B) represent data from guinea pig islets, and the hatched bar represents data from bovine chromaffin cells. The molecular dimensions of the various tracers are shown in nanometers, and their relative sizes are indicated schematically as circles. (**F**) Fusion event detected with SRB that was not accompanied by an increase in staining with 10-kD fluorescein-dextran. (**G**) Simultaneous staining of an insulin granule with SRB and 70-kD fluorescein-dextran. (**H**) Latency histogram for the onset of SRB decay (SRB_{peak}) relative to the opening of the large pore that allows the permeation of 70-kD fluorescein-dextran.

diffusion of secreted substances and promotes paracrine interactions within the islet, where β, α, and δ cells tend to be segregated (*14*).

Our data suggest the notion (*24*, *28*) that the fusion pore of physiological exocytosis is formed by membrane lipids whose lateral diffusion is not prevented by immobile proteins (*23*). If the initial pore is formed from proteinaceous channels (*3*, *10*), such channels would have to be disassembled before expansion of the pore to a diameter of 1.4 nm so as not to prevent lipid diffusion. Thus, the role of fusogenic proteins is more likely to be to control the proximity of two biological membranes and thereby to facilitate formation of the lipidic nanopore. Such proteins may prevent lipid flux along the outer wall of the fusion pore, as described for hemagglutinin-induced cell fusion (*29*); the outer wall of the fusion pore might thus be proteinaceous to some extent. Given that insulin secretion is mediated by an expanding lipidic pore, abnormal lipid metabolism (*14*) in individuals with non–insulin-dependent (type 2) diabetes mellitus may impair secretion at the level of lipidic pore structure. Our approach provides a means of further elucidating the molecular control of fusion pore structures during physiological exocytosis.

References and Notes

1. E. Neher, *Neuron* **20**, 389 (1998).
2. L. J. Breckenridge, W. Almers, *Nature* **328**, 814 (1987).
3. J. Zimmerberg, M. Curran, F. S. Cohen, M. Brodwick, *Proc. Natl. Acad. Sci. U.S.A.* **84**, 1585 (1987).
4. G. Alvarez de Toledo, R. Fernadez-Chacon, J. M. Fernandez, *Nature* **363**, 554 (1993).
5. Z. Zhou, S. Misler, R. H. Chow, *Biophys. J.* **70**, 1543 (1996).
6. L. Orci, M. Amherdt, F. Malaisse-Lagae, C. Rouiller, A. E. Renold, *Science* **179**, 82 (1973).
7. H. Plattner, A. R. Artlejo, E. Neher, *J. Cell Biol.* **139**, 1709 (1997).
8. D. E. Chandler, J. E. Heuser, *J. Cell Biol.* **86**, 666 (1980).
9. T. Kanaseki, K. Kawasaki, M. Murata, Y. Ikeuchi, *J. Cell Biol.* **137**, 1041 (1997).
10. J. Zimmerberg, *Trends Cell Biol.* **11**, 233 (2001).
11. W. Denk, J. H. Strickler, W. W. Webb, *Science* **248**, 73 (1990).
12. Materials and methods are available as supporting material on *Science* Online.
13. T. Nemoto *et al.*, *Nature Cell Biol.* **3**, 253 (2001).
14. C. R. Kahn, G. C. Weir, *Joslin's Diabetes Mellitus* (Lea & Febiger, Phildelphia, PA, 1994).
15. N. Takahashi *et al.*, *Proc. Natl. Acad. Sci. U.S.A.* **96**, 760 (1999).
16. L. Orci, M. Ravazzola, R. G. Anderson, *Nature* **326**, 77 (1987).
17. W. J. Qian, C. A. Aspinwall, M. A. Battiste, R. T. Kennedy, *Anal. Chem.* **72**, 711 (2000).
18. S. Bonner-Weir, *Diabetes* **37**, 616 (1988).
19. D. G. Pipeleers, *Diabetes* **41**, 777 (1992).
20. N. Takahashi, T. Kadowaki, Y. Yazaki, Y. Miyashita, H. Kasai, *J. Cell Biol.* **138**, 55 (1997).
21. W. J. Betz, F. Mao, G. S. Bewick, *J. Neurosci.* **12**, 363 (1992).
22. N. Takahashi *et al.*, *Diabetes* **51** (suppl. 1), S25 (2002).
23. T. Fujiwara, K. Ritchie, H. Murakoshi, K. Jacobson, A. Kusumi, *J. Cell Biol.* **157**, 1071 (2002).
24. J. R. Monck, G. Alvarez de Toledo, J. M. Fernandez, *Proc. Natl. Acad. Sci. U.S.A.* **87**, 7804 (1990).
25. G. Dodson, D. Steiner, *Curr. Opin. Struct. Biol.* **8**, 189 (1998).
26. S. Barg *et al.*, *Neuron* **33**, 287 (2002).
27. P. A. in't Veld, D. G. Pipeleers, W. Gepts, *Diabetes* **33**, 101 (1984).
28. A. Chanturiya, L. V. Chernomordik, J. Zimmerberg, *Proc. Natl. Acad. Sci. U.S.A.* **94**, 14423 (1997).
29. F. W. Tse, A. Iwata, W. Almers, *J. Cell Biol.* **121**, 543 (1993).

30. We thank H. Gaisano for critical reading of the manuscript; H. Noguchi for helpful discussion; and R. Ijuin, T. Kise, and N. Takahashi for technical assistance. This work was supported by Grants-in-Aid from the Japanese Ministry of Education, Culture, Sports, Science and Technology and the Japan Society for the Promotion of Science; by Research grants from the Human Frontier Science Program Organization, Uehara Memorial Foundation (H.K.), and Japan Diabetes Foundation (N.T.); and by PRESTO of the Japan Science and Technology Corporation (JST) (T.N.).

Supporting Online Material

www.sciencemag.org/cgi/content/full/297/5585/1349/DC1
Materials and Methods
Supporting Text
Figs. S1 and S2
Movies S1 and S2

10 May 2002; accepted 28 June 2002

Requirement for Caspase-2 in Stress-Induced Apoptosis Before Mitochondrial Permeabilization

Patrice Lassus, Ximena Opitz-Araya, Yuri Lazebnik*

A current view is that cytotoxic stress, such as DNA damage, induces apoptosis by regulating the permeability of mitochondria. Mitochondria sequester several proteins that, if released, kill by activating caspases, the proteases that disassemble the cell. Cytokines activate caspases in a different way, by assembling receptor complexes that activate caspases directly; in this case, the subsequent mitochondrial permeabilization accelerates cell disassembly by amplifying caspase activity. We found that cytotoxic stress causes activation of caspase-2, and that this caspase is required for the permeabilization of mitochondria. Therefore, we argue that cytokine-induced and stress-induced apoptosis act through conceptually similar pathways in which mitochondria are amplifiers of caspase activity rather than initiators of caspase activation.

Apoptosis is executed by caspases, a family of proteases that disassemble a cell (*1*, *2*). The pathways leading to caspase activation vary with the cytotoxic stimulus. The stimuli that are collectively referred to as cytotoxic stress, such as DNA damage, activate caspases by initiating signaling pathways that converge on the Bcl-2 family of proteins (*3*). A balance between members of this family is thought to determine whether mitochondria remain intact or become permeabilized and release proteins that promote cell death (*4*). One of these released proteins is cytochrome c, which, in a complex with the cytoplasmic protein Apaf-1, activates caspase-9. Caspase-9, in turn, activates caspase-3, the protease that cleaves the majority of caspase substrates during apoptosis. Two other proteins, Smac (also called Diablo) and Htr2A (Omi), accelerate caspase activation and increase caspase activity by inactivating caspase inhibitors. Mitochondria also release apoptosis- inducing factor (AIF) and endonuclease G, which appear to kill independently of caspases. Therefore, mitochondria are thought to be a central regulatory element in stress-induced apoptosis (*5*).

Another way to activate caspases, used by cytokines, is to assemble receptor complexes that recruit caspase-8 or caspase-10, thereby inducing their autocatalytic processing (*2*). These caspases activate other caspases, including caspase-3, either directly (by proteolytic processing) or indirectly by cleaving Bid, a Bcl-2 family member. A proteolytic fragment of Bid permeabilizes mitochondria, thereby accelerating cell disassembly as described above. Hence, mitochondria in this pathway function as "amplifiers" of the caspase activity rather than as central regulators of apoptosis.

This model of apoptosis was consistent with studies of oncogene-dependent apoptosis, a phenomenon that may provide clues about how to kill cancer cells selectively (*6*). By comparing normal human fibroblasts (IMR90) with fibroblasts transformed with the adenoviral oncogene *E1A* (IMR90E1A), we found that this oncogene sensitizes cells to chemotherapeutic drugs by facilitating the activation of caspase-9 (*7*). *E1A* appears to achieve this effect by promoting the activation of Bax, a proapoptotic Bcl-2 protein that can permeabilize mitochondria, and by repressing a still-unidentified inhibitor of this permeabilization (*8*). These observations were in agreement with a model in which Bcl-2 proteins control caspase activation by regulating mito-

Cold Spring Harbor Laboratory, Cold Spring Harbor, NY 11724, USA.

*To whom correspondence should be addressed. E-mail: lazebnik@cshl.org